

A method for generating patient-specific finite element meshes for head modelling

A P Gibson¹, J Riley², M Schweiger², J C Hebden¹, S R Arridge²
and D T Delpy¹

¹ Department of Medical Physics and Bioengineering, University College London, UK

² Department of Computer Science, University College London, UK

Received 28 November 2002

Published 5 February 2003

Online at stacks.iop.org/PMB/48/481

Abstract

Finite element modelling of fields within the body, whether electrical or optical, requires knowledge of the geometry of the object being examined. It can be clinically impractical to obtain accurate surface information for individual patients, although a limited set of measurements such as the locations of sensors attached to the body, can be acquired more readily. In this paper, we describe how a generic surface taken from an adult head is warped to fit points measured on a neonatal head surface to provide a new, individual surface from which a finite element mesh was generated. Simulations show that data generated from this mesh and from the original neonatal head surface are similar to within experimental errors. However, data generated from a mesh of the best fit sphere were significantly different from data generated from the original neonatal head surface.

1. Introduction

In some medical imaging techniques, each measurement depends on the tissue properties within a limited, well defined projection through the body. For example, in computed tomography (CT), the x-ray beam travels in a straight line. The image reconstruction can then be expressed as a Radon transform and it is straightforward to generate an image using methods such as filtered backprojection. In other imaging techniques, the probing field tends to distribute itself throughout the volume, making each measurement sensitive to a large part of the body under examination. If this is the case, a Radon transform does not exist and image reconstruction is, therefore, more difficult and should be approached as an inverse problem (Arridge 1999, Arridge and Hebden 1997). These techniques are sometimes referred to as 'soft-field' imaging techniques and include electroencephalographic (EEG) inverse source localization, magnetoencephalography (MEG), electrical impedance tomography (EIT) and optical tomography (OT).

In these methods, the distribution of the field must be found by solving an appropriate numerical model, typically using either the boundary element method (BEM) or the finite element method (FEM). Both of these need a description of the surface of the body which is then discretized to give either a surface or a volume mesh. This mesh should accurately represent the body shape of the patient being imaged. Obtaining an individual mesh of each subject, however, can be time-consuming or clinically impracticable.

A surface outline can be obtained using magnetic resonance imaging (MRI) or CT, but it is inconvenient and often, particularly in the case of neonates, clinically unjustifiable to obtain CT and even MR images of every subject. Commercial EEG inverse source localization programs such as ASA (www.ant-software.nl/asa/) and CURRY (www.neuro.com/neuroscan/prod05.htm) are supplied with a library of standard MR images of the head and the user selects the model which is most similar to the patient. Increasingly, researchers are using anatomically realistic finite element models based on MR or CT images for modelling and image reconstruction. Recent reports include Dimbylow (2002) who used a high-resolution finite difference time domain model of the head to simulate the dose received from a microwave transmitter, Ermer *et al* (2001) who used a realistic boundary element model for EEG forward modelling and Pogue *et al* (2001) who used a realistic breast model for optical tomography reconstruction. Other methods which have been used to provide patient-specific surfaces include using stereo photogrammetry (Bluestone *et al* 2001), a mechanical 3D digitizing arm (Gibson 2000), a 3D digitizer which detects the position of a stylus with a magnetic field (Nishitani *et al* 1999) and 3D laser scanners, which are already used clinically in radiotherapy and stereotaxic applications.

All these methods involve generating a patient-specific surface directly. They are more convenient to use than MRI but still require a compliant patient, which may not be the case, especially for neonates in intensive care. Our approach is to generate the surface indirectly, by warping the known surface of a similar object to fit a sparse set of points measured on the patient. This provides a new surface which passes through the measured points from which a finite element mesh can be generated for modelling. This approach is similar to medical image registration, where an entire 2D or 3D image is warped to fit another image or dense set of points (Hill *et al* 2001).

In this paper, we show specifically how a volume mesh suitable for modelling the head of an individual infant can be generated by warping a generic surface to fit a set of target points, which are taken to be the measured locations of sensors attached to the head. The technique was developed for optical tomography, where the positions of approximately 30 optodes held in a rigid helmet are known (Hebden *et al* 2002). The method is appropriate for any imaging modality where a generic surface can be obtained and the positions of a group of points on the surface are known.

2. Experimental method

A generic head-shaped surface was obtained from a tissue-equivalent phantom, constructed for use in optical tomography. The phantom was cast in epoxy resin (Firbank *et al* 1995) from a mould made from an anatomically realistic doll. The circumference was 24 cm, corresponding to a baby of about 26 weeks gestation. A 3D CT scan of the phantom was taken with a spatial resolution of about 0.5 mm (Gibson *et al* 2003). The surface of the phantom was extracted using software written in-house (www.medphys.ucl.ac.uk/research/mgi/manual/3dintro.htm) which treats the CT image as an array of greyscale voxels. The phantom surface was defined as an interpolated iso-surface through the voxel array at a threshold which was set about halfway

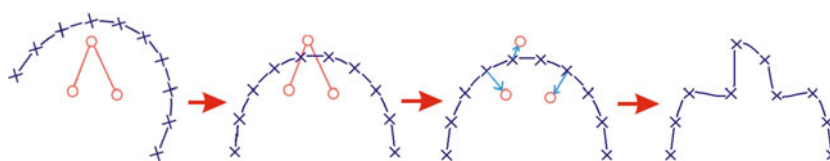


Figure 1. A schematic diagram showing the warping process. The blue semicircle with crosses represents a generic surface with nodes placed at the crosses. The red triangle denotes the positions of three measured points. From left: (1) the generic surface and measured points are known to the same scale, but their relative positions are unknown; (2) the generic surface is linearly rotated, translated and stretched to fit the measured points; (3) the nearest node on the generic surface to each measured point is identified; (4) the warp is applied to generate a new surface which passes through the measured points.

between the mean greyscale value inside the phantom and that outside. The surface was stored as a triangular mesh, and then smoothed and decimated using the Visualization Toolkit (VTK, Kitware, Inc., USA) to give a triangulated surface mesh with 1437 nodes and 2872 elements.

Our first optical tomography measurements on infants (Hebden *et al* 2002) used a rigid helmet to hold the optodes in place on the head and provide light insulation. The positions of the optodes on the helmet were measured using a 3D digitizing arm (Microscribe 3D, Immersion Corp., USA) which gave their positions accurate to about 0.5 mm. To provide a surface which fitted these points, the surface acquired from the phantom was warped to fit the measured optode positions.

The warping was applied in three stages (see figure 1):

- The surface was translated, rotated and stretched linearly in all three directions so that the ear-to-ear distance on the mesh was equal to the maximum left–right distance between the optodes.
- The closest nodes on the surface mesh to each optode were identified. The nearest nodes cannot always be reliably identified around irregular and concave regions such as the eyes, nose and throat. In practice, however, these regions are too far from the optodes to affect the quality of the warp. The initial linear stretch of the surface ensured that this registration was robust—if the surface was much smaller than that defined by the optode positions, the nearest node to each optode was highly sensitive to the shape of the head.
- A nonlinear thin-plate spline transform (Bookstein 1989) was applied to the initial surface so that the surface nodes (known as the source nodes) were warped to the measured optode positions (the target nodes). This was also implemented in VTK.

The thin-plate spline is the interpolation function which passes through all the points, whilst minimizing the bending energy, I , expressed as the integrated square of the second derivatives. This is shown below in equation (1), where z is the height of the surface above the (x, y) plane

$$I(x, y) = \iint \left(\frac{\partial^2 z}{\partial x^2} \right)^2 + 2 \left(\frac{\partial^2 z}{\partial x \partial y} \right) + \left(\frac{\partial^2 z}{\partial y^2} \right) dx dy. \quad (1)$$

The result was a surface which maintained the features of the initial outline but passed through the optode positions measured on the baby. Finally, a volume mesh (figure 2) was generated using Netgen (Schöberl 1997). Generating a new volume mesh from the warped surface provides a better quality volume mesh than simply 3D warping of an existing mesh as

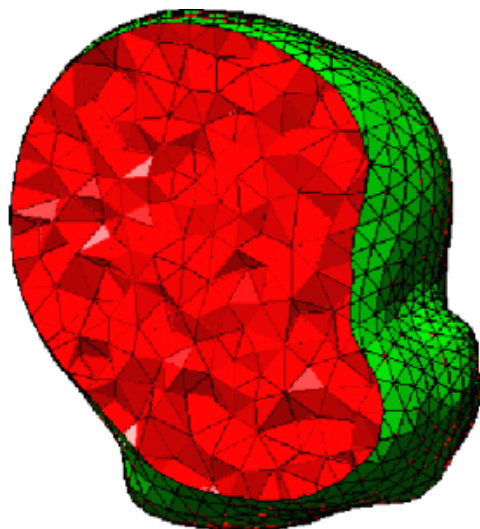


Figure 2. Structure of a typical finite element mesh of the neonatal head used in this work.

this can lead to distorted elements. This method was successfully used to provide the finite element mesh for the first 3D optical tomography images of the neonatal brain (Hebden *et al* 2002).

3. Method of validation

3.1. Overview

The technique outlined above was used to warp a generic surface to measured points. However, the quality of the warp cannot be quantified because the correct target surface is unknown. To validate the technique, the warped surface must be compared to a different known surface. Therefore, the neonatal head shaped phantom surface described above was used as the target surface rather than the source and a second surface, taken from an MR image of an adult head, was warped to fit it. This ensured that the warped source surface could be directly compared to the original target surface and gave a more extreme test of the quality of the warp than would be encountered clinically, when a generic surface from a baby head is warped to a specific infant. In addition, the sphere which gave the best least-squares fit to the measured points using a Gauss–Newton fitting algorithm (www.npl.co.uk/ssfm/metros/key_functions/fitting_routines/) was used as a second comparison.

The three surfaces were compared directly and finite element meshes were generated from each. Data were simulated to allow the performance of the three surface generation techniques to be compared. Although the warping technique is not specific to any one medical imaging method, the first intended use is in optical tomography. Our optical tomography system (Schmidt *et al* 2000) measures the transit times of individual photons which have travelled through the body, from which we calculate the total transmitted intensity and the mean photon flight time (Hillman *et al* 2000). In this work, we generated simulated intensity and mean time data following the same protocol as was used for the neonatal brain imaging discussed above. This employed 29 optodes, each consisting of a source fibre and a detector fibre bundle (Hebden *et al* 2003), and gave a total of 678 measurements. These points acted both as the

source and measurement points and as the target points for the warp. The separation between the source–detector pairs used for data acquisition ranged from 15 mm to 77 mm.

3.2. Generation of multiple surface meshes

To allow data simulated for the three surfaces to be compared with each other statistically, approximately 50 finite element meshes were generated from each surface and data were simulated for each. First, multiple surface meshes were generated using VTK by controlling the number of neighbours each node has and by changing the spacing of the 3D sampling grid used in the surface reconstruction algorithm (see www.vtk.org/doc/release/4.0/html/classvtkSurfaceReconstructionFilter.html for details). This gave 23, 20 and 33 different surface meshes for the neonatal head phantom, the warped adult head and the sphere, respectively, with an average of 1601, 1596 and 2028 nodes.

3.3. Generation of multiple volume meshes

Volume finite element meshes (see figure 2) were generated from the surface meshes using Netgen (Schöberl 1997). A range of volume meshes, each respecting the original surface mesh, was generated by controlling a quantity known as the ‘fineness’ (see Schöberl (1997) for details). Any meshes with fewer than 1000 or more than 5000 nodes were rejected. Each mesh was then converted to a mesh with quadratic interpolation functions by adding extra nodes at the midway point of each edge, and any meshes with fewer than 15 000 or more than 30 000 nodes were rejected. Finally, to exclude any possibility of duplicate meshes, any mesh which had the same number of nodes as an existing mesh was rejected. The background properties of all the meshes were set to an absorption coefficient of $\mu_a = 0.01 \text{ mm}^{-1}$ and a transport scatter coefficient of $\mu'_s = 1.0 \text{ mm}^{-1}$. Two 5 mm diameter spherical perturbations were added to each mesh, one with five times the background absorption and the other with five times the background scatter (figure 3). Any meshes with fewer than ten nodes in either perturbation were rejected. This left 46, 67 and 30 different volume finite element meshes for the neonatal head, warped adult and the spherical surfaces, respectively, with an average of $19\,300 \pm 3000$, $20\,100 \pm 3000$ and $20\,600 \pm 4000$ tetrahedral elements with quadratic interpolation functions. Any one of these meshes would have been suitable for image reconstruction.

3.4. Data simulation

One final check was performed on each mesh by generating a map of the photon density throughout each mesh using the TOAST optical tomography modelling and reconstruction program developed at UCL (Arridge *et al* 2000). A poor-quality finite element mesh typically produces negative photon densities at some nodes. These must be erroneous, so rather than constraining the photon densities to be positive, we rejected two meshes which produced negative photon densities. Intensity and mean photon flight time data were then calculated using TOAST for each of the remaining finite element meshes, both with and without the simulated optical perturbations.

3.5. Comparison of surface geometries

The warped adult head and the spherical source surfaces were each compared to the target neonatal head surface using a measure based on the Hausdorff distance. The Hausdorff distance, H , between two sets of points $P = \{p_1, \dots, p_n\}$ and $Q = \{q_1, \dots, q_m\}$ is shown in

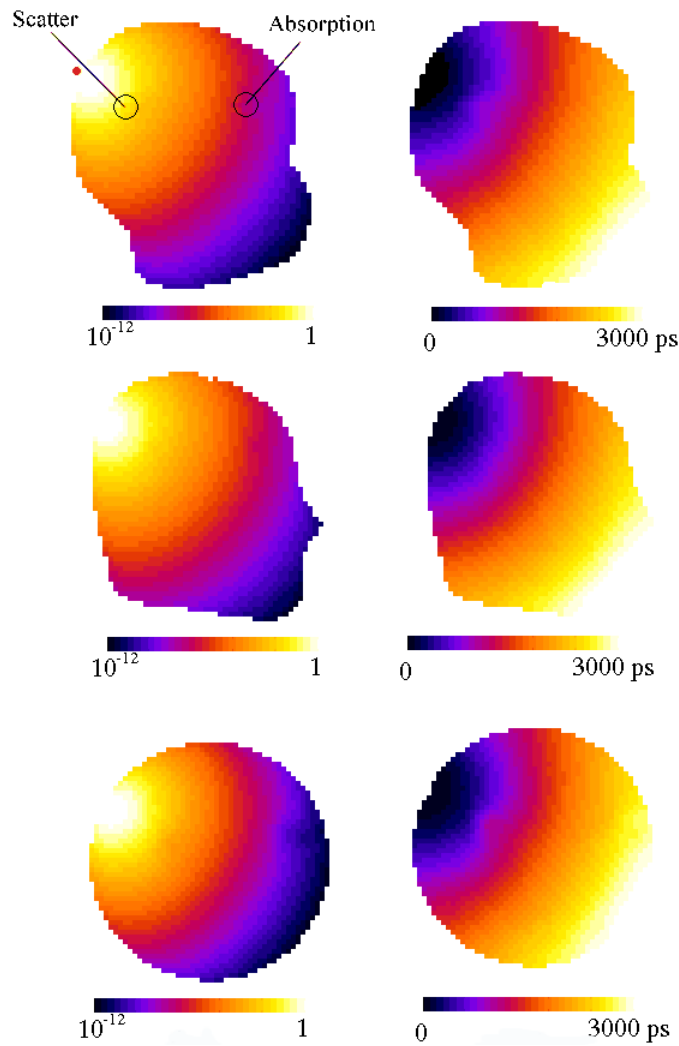


Figure 3. Simulated maps of log of photon intensity (left-hand column) and mean photon flight time (right-hand column) using a single source optode position, denoted by the red dot in the top left figure, for the three meshes used. The locations of the two spherical perturbations are shown as circles. The top row corresponds to the neonatal head mesh, the middle row the warped adult head (middle) and the bottom row the best-fit sphere. The intensity decreases smoothly from the source position over 12 orders of magnitude, and the mean photon flight time increases approximately linearly with distance.

equation (2) where $h(P, Q) = \min_{q \in Q} \|p - q\|$ and $\|\cdot\|$ is the L_2 norm of the points in P and Q . The Hausdorff distance is, therefore, the maximum distance separating any node in one mesh from its closest node in the other mesh (Huttenlocher *et al* 1993). Note that $H(P, Q)$ is not symmetric

$$H(P, Q) = \max \left(\max_{p \in P} (h(p, Q)), \max_{q \in Q} (h(q, P)) \right). \quad (2)$$

In this work, the Hausdorff number itself is not a useful measure of similarity between the two surfaces as the greatest distance between them occurs at the nose and the neck, which

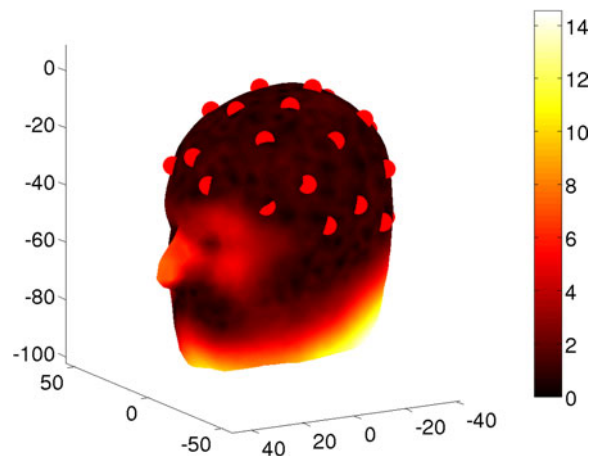


Figure 4. Absolute undirected Hausdorff distance, $h(P, Q)$, between warped adult head surface, P , and surface of neonatal head phantom, Q , in mm; see equation (1).

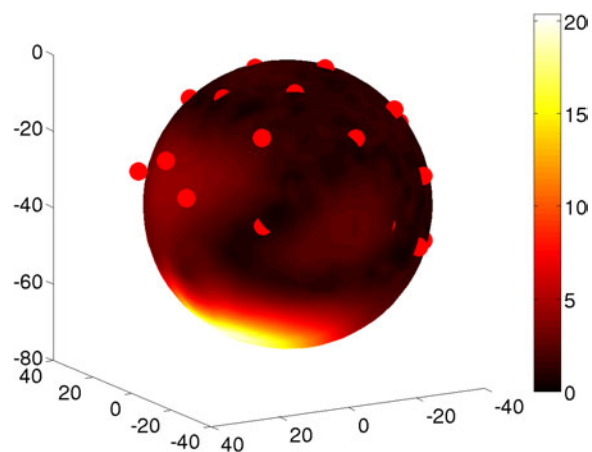


Figure 5. Distance between best fit spherical surface and surface of neonatal head phantom in mm.

have little effect on data simulation. Instead, $h(P, Q)$, the undirected Hausdorff distance, was calculated for every node on the source mesh and displayed on the source mesh itself. The results are shown as figures 4 and 5 which can be interpreted as plots of the source mesh surface, with the colour scale given by the absolute distance from each node in the source mesh to the nearest node on the target mesh.

3.6. Comparison of simulated data

Data simulated from a warped surface and the original target surface will not be identical. To test the quality of the warp in a useful way, we need to ask whether the data from the warped mesh is 'good enough'. A measure of the quality of the warp was provided by generating many finite element meshes for each surface so that differences between data generated from two meshes can be compared to the statistical variation from the different meshes.

Data were simulated for approximately 50 meshes for each of the three surfaces being investigated. Each simulated measurement could then be represented by a sample distribution with a mean and a standard deviation. Standard statistical methods can then be used to compare data generated from the source surface to data generated from the target. However, care must be taken for two reasons. First, the data in each sample are not normally distributed. Second, we know *a priori* that the two samples being compared come from two different populations: the data were generated from two different surfaces. This means that we cannot expect the data to agree to within the usual statistical tolerances. In this work, Student's *t*-test was used to compare a sample distribution from the source surface to that calculated from the target surface. Rather than using the *t*-test as a binary measure of 'significant' or 'not significant,' it was used as a measure of agreement between the two distributions. There are 678 different simulated measurements in each dataset, so the outcome is 678 different *t*-tests for each of the two source surfaces. A *t*-test between two distributions is commonly performed to a significance level of 5%, which means that the probability of obtaining those two distributions, if they actually come from the same population, is 5%. This leads, by definition, to a 5% false positive rate, i.e. if 100 *t*-tests are performed on two distributions which were taken from the same sample, five will indicate erroneously that the two distributions are different. Therefore in this case, where we perform 678 *t*-tests, we would expect 34 to give $p < 0.05$, even if the two distributions are the same.

4. Results

4.1. Adult head surface warped to baby head

The adult head surface was warped to fit the optode positions measured on the neonatal head-shaped phantom. The absolute distance between each node in the source surface and its nearest neighbour in the target ($h(P, Q)$ in equation (2)) was calculated and displayed for every node (figure 4). A measure of the quality of the warp was provided by taking the mean $h(P, Q)$ for all nodes where $z > -40$ mm, approximately corresponding to the upper half of the head to which the optodes were attached. The mean distance was (1.2 ± 0.5) mm and the maximum was 3.7 mm. The maximum distance between an optode on the neonatal head surface and the nearest surface node on the warped adult head surface was 1.0 mm.

4.2. Sphere fitted to baby head

The radius of the best-fit sphere was 36.9 mm. $h(P, Q)$ was found for each node and plotted, as before (figure 5). The mean $h(P, Q)$ for all nodes where $z > -40$ mm was (1.5 ± 0.9) mm and the maximum was 4.6 mm. The maximum distance between an optode and the nearest surface node was 3.1 mm.

4.3. Absolute forward simulations

Figure 3 shows sagittal slices through 3D volume maps of the log of the photon intensity and the mean photon flight time calculated from each of the three surface types. The general features of the simulated fields in the three meshes are similar, but the details differ.

A mean simulated dataset was produced for each of the three surfaces by averaging the simulated datasets generated from the repeated finite element meshes. An absolute comparison between the different surfaces was obtained by examining the root-mean-square difference between the 678 simulated mean photon flight times for the source surface and the target surface. The absolute mean difference between the warped adult and the neonatal

head shaped surfaces was 10 ± 7 ps ($0.7 \pm 0.5\%$), with a maximum of 32 ps (4%). The mean difference between the spherical and the neonatal head shaped surfaces increased to 32 ± 28 ps ($2.1 \pm 1.5\%$), and the maximum to 126 ps (11%).

A Student's *t*-test was performed on each pair of simulated measurements, giving 678 *t*-tests. When the data from the warped adult head surface were compared to those from the neonatal head surface, 565 *p*-values were less than 0.05 for intensity measurements and 479 were less than 0.05 for mean photon flight time measurements. For the comparison between the sphere and the neonatal head surface, 579 intensity and 567 mean flight time *p*-values were less than 0.05.

4.4. Difference simulations

The final series of tests was performed on difference data, that is either (a) the ratio of simulated intensity measurements with the perturbations in place to measurements simulated on a geometrically identical mesh with homogeneous parameters, or (b) the difference in mean photon flight times with and without the perturbations. This enables the effect of the perturbations on the measurements to be examined. The results are plotted in figures 6 and 7. Most measurements have little sensitivity to a particular localized perturbation and so record no detectable change. For this reason, the mean change has little practical meaning, and the maximum is more meaningful. The maximum intensity ratio for data simulated using meshes generated from the neonatal head shaped surface with and without the perturbations was 0.642, and the maximum mean photon flight time difference was 45 ps.

As before, Student's *t*-test was performed on every pair of simulated measurements. Comparing data from the warped adult surface with the neonatal baby surface showed that 102 and 78 *p*-values were less than 0.05 for the intensity measurements and mean flight time measurements, respectively. When the spherical surface was compared to the neonatal head surface, 161 intensity measurements and 269 mean flight time measurements gave *p*-values less than 0.05.

5. Discussion

5.1. Comparison of three surfaces

The mean difference between the upper part of the warped adult head surface or the spherical surface and the upper part of the neonatal head surface was little more than 1 mm. This is similar to the node separation and can, therefore, be assumed to be due primarily to discretization effects. Similarly, the maximum distance between an optode on the warped adult surface and the nearest node on the neonatal head surface was 1.0 mm, which demonstrates that the adult head surface was warped to fit the optode positions successfully. This compares with the spherical surface where in the worst case an optode lay 3.7 mm from the surface.

5.2. Reproducibility of data generated using repeated finite element models.

Repeated finite element meshing of the same object enables the uncertainties caused by the finite element method to be examined. Figure 8 shows intensity and mean flight time data plotted for a measurement from a single source–detector pair (the pair with the median source–detector separation, which was 52.7 mm) for all the repeated meshes for each of the three surfaces. Two important conclusions can be drawn from this figure. First, there is a significant spread in results obtained from repeated finite element meshes of the same object. Indeed,

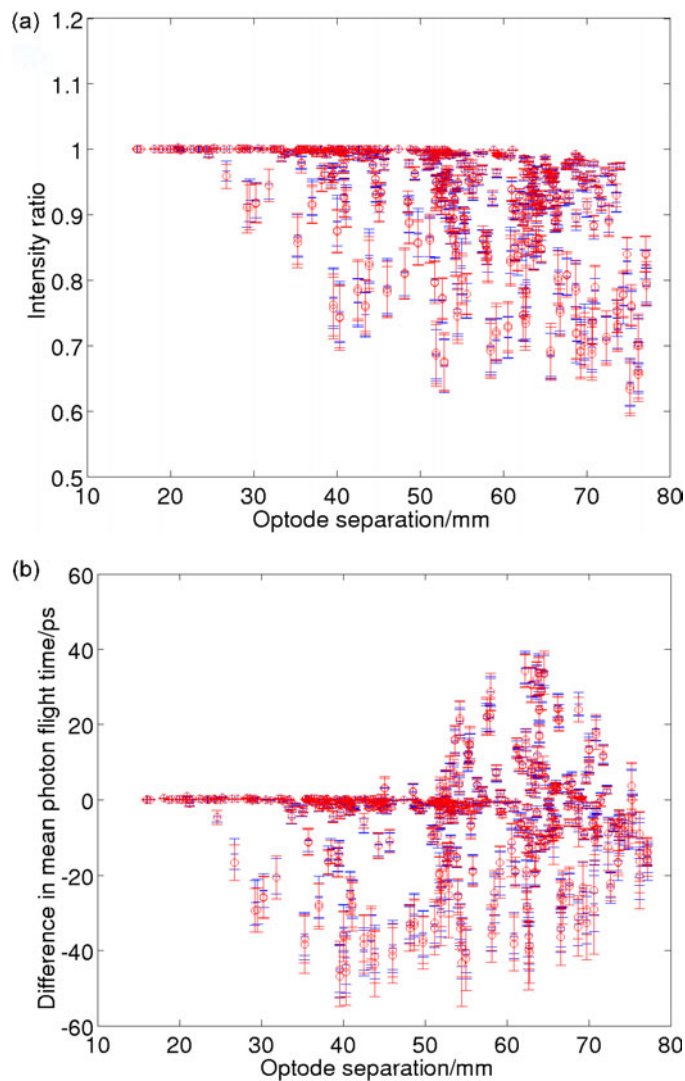


Figure 6. Data were simulated on repeated finite element meshes, providing a distribution for each of 678 simulated measurement positions: (a) the mean \pm standard deviation of each simulated intensity measurement distribution, expressed as the ratio of the intensity with the two perturbations to that obtained from the homogeneous mesh; (b) the mean \pm standard deviation difference in simulated mean photon flight times with and without the perturbations. Data simulated for the neonatal head surface are shown in blue and the warped adult head mesh in red.

the spread in mean photon flight times is about 100 ps, which is considerably more than the simulated change due to the perturbations. This supports the proposition that absolute imaging is highly sensitive to modelling errors. For difference imaging, where images of the difference between two states are reconstructed, these modelling errors are common to both states and will largely cancel. Second, it can clearly be seen that data obtained from the neonatal head surface overlap considerably with data from the warped adult head, but that data from the spherical meshes appear to be different. The substantial overlap between data generated from the neonatal baby surface and the adult was common to all the measurements, but the difference

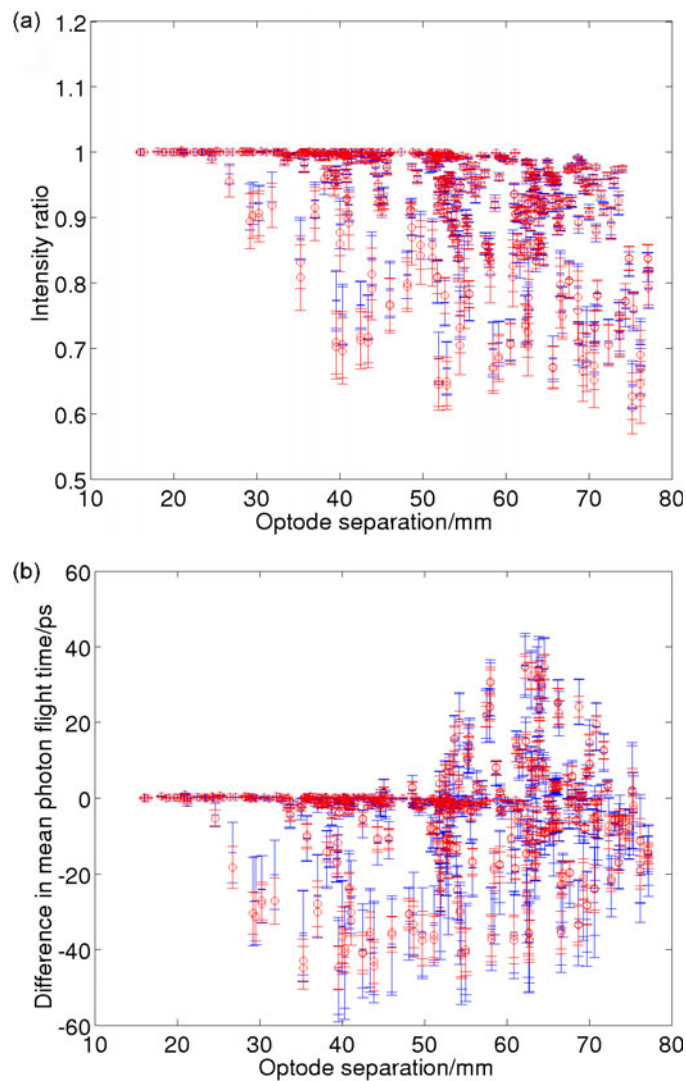


Figure 7. Same as for figure 6, again showing (a) simulated intensity measurement distributions and (b) mean photon flight times, with and without the two perturbations. Data simulated for the neonatal head surface are shown in blue and the spherical mesh in red.

between data from the spherical surface and the neonatal head shaped surface increased as the source–detector separation increased.

5.3. Comparison of absolute error

Forward simulations (see table 1) showed that the average errors in mean photon flight time were 10 ± 7 ps (maximum 32 ps) between the warped adult head surface and the neonatal head surface, and 32 ± 28 ps (maximum 128 ps) between the spherical surface and the neonatal head surface. Two perturbations, whose volume and optical properties are expected to be similar to a small clinical lesion, were added. They introduced a change in mean photon flight

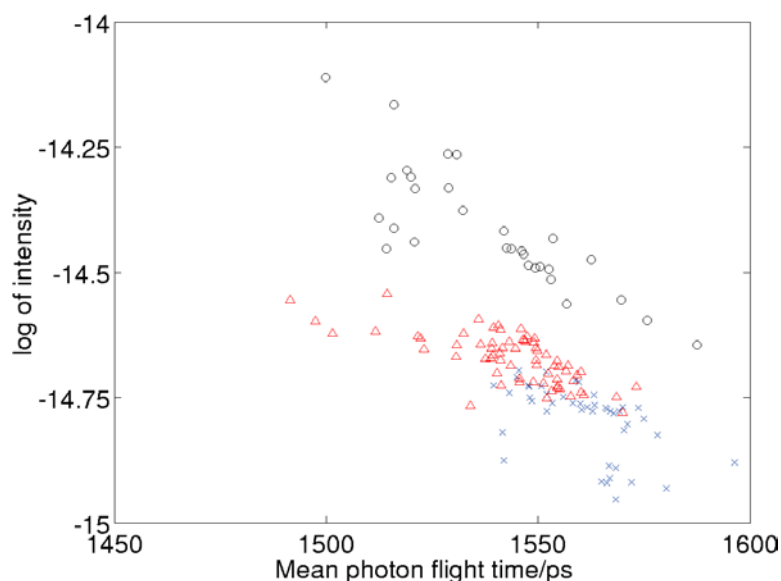


Figure 8. Log intensity plotted against mean photon flight time for a single measurement (that with the median source–detector separation) simulated from repeated meshes of the same object, showing the spread in results due to uncertainties in the finite element modelling process. Blue crosses: data simulated from the neonatal head shaped phantom, red triangles: data simulated from the warped adult surface, black circles: data simulated from the sphere.

Table 1. Summary of results discussed in the text. The data are averaged from 46 different finite element meshes of the neonatal head, 67 for the warped adult head and 30 spherical meshes. An image dataset of 678 measurements was simulated for each mesh.

	Warped adult head surface compared to neonatal head surface	Best fit spherical surface compared to neonatal head surface
Average difference in mean photon flight time/ps	10 ± 7	32 ± 28
Maximum difference in mean photon flight time/ps	32	128
Absolute intensity <i>t</i> -test	565 <i>p</i> -values < 0.05	579 <i>p</i> -values < 0.05
Absolute mean photon flight time <i>t</i> -test	479 <i>p</i> -values < 0.05	567 <i>p</i> -values < 0.05
<i>t</i> -test between intensity ratios with and without perturbation	102 <i>p</i> -values < 0.05	161 <i>p</i> -values < 0.05
<i>t</i> -test between mean photon flight times difference with and without perturbation	78 <i>p</i> -values < 0.05	269 <i>p</i> -values < 0.05

time of up to 45 ps. This suggests that the error introduced by warping an adult head surface to fit the neonatal head surface is less than the expected signal size, but that the error caused by using a spherical surface could be significantly larger than the effect of the perturbation. The same analysis could be performed on the intensity datatype but, due to the very large dynamic range in the number of photons detected (typically 10^9), the uncertainty in intensity

measurement is dominated by photon counting statistics and the variable coupling between the optode and the skin surface (Hebden *et al* 2003) and is therefore more difficult to quantify reliably.

5.4. Statistical comparison

When image datasets of absolute intensity and mean photon flight time simulations for both the warped adult head and the spherical surfaces were compared to the neonatal head surface, more than 70% of the *t*-tests gave *p*-values less than 0.05. If the two sets of distributions were identical, only 5% would be expected to be less than this threshold. The fact that some of the measurements are statistically indistinguishable from each other suggests that the warped and spherical meshes produce data which appear to be similar but not identical to the neonatal head phantom.

Difference data is generally assumed to be less sensitive than absolute imaging to modelling errors, including both uncertainty in the true geometry and inherent errors introduced by the modelling process. Indeed, only 102 *t*-tests between intensity ratio measurements and 78 *t*-tests for mean flight time measurements gave *p*-values less than 0.05 (15% and 11.5%, respectively) when the warped adult head surface was compared to the neonatal head surface. This suggests that the data from the warped mesh do faithfully represent the data from the neonatal head mesh, though there are rather more outliers than would be expected if they came from the same distribution. This is not surprising, as the two meshes are clearly different.

For the spherical mesh, the corresponding results show that 161 intensity ratio and 269 mean flight time measurements give *p*-values less than 0.05 (24% and 40%), again suggesting that whilst there is some agreement between the two sets of data, a substantial number of measurements give results which would contribute to image artefacts.

6. Conclusions

The tests outlined above suggest that the spherical mesh could not be used to accurately model either absolute or difference data. More than 70% of the measurements from the sphere were statistically different from measurements from the neonatal head model, and figure 8 shows that this difference was substantial. The uncertainty with which our optical tomography system can measure the mean photon flight time is approximately 10–20 ps (Hebden *et al* 2001) and the *average* difference between the two datasets was greater than this—the maximum difference was up to ten times larger. Even in the case of difference data, which is much more robust to modelling errors, more than a quarter of the measurements were statistically different from the equivalent measurements obtained from the neonatal head model. This supports previous work in both optical and impedance imaging. In optical tomography of the neonatal head shaped phantom used in this work (Gibson *et al* 2003), images obtained using a realistic mesh showed fewer artefacts than those obtained using a spherical mesh. Similarly, in impedance imaging, whilst difference images can be reconstructed from data acquired on the adult head using a spherical mesh, artefacts are introduced into the image (Tidswell *et al* 2001) which are reduced if a realistic mesh is used (Bagshaw *et al* 2003). Furthermore, this confirms that data simulated on the neonatal head model do correspond more closely to data measured on such a phantom than results simulated on the spherical mesh.

Similarly, 70% of data simulated on the warped adult mesh were statistically different from data simulated on the neonatal head model. However, the difference was similar in size to the uncertainty in the measurement of meantime and, given that warping an adult head to fit the neonatal head is an extreme test, it is conceivable that this method could be used for

accurate absolute forward modelling. However, figure 8 suggests that errors caused by the finite element method itself may dominate during the calculation of absolute data. This result was unexpected and deserves further study.

These results support the use of a warped mesh for modelling difference data: the difference between data simulated from the warped adult mesh and the neonatal mesh was less than the size of the expected measured perturbation and only two or three times more measurements were statistical outliers than would have been expected by chance. Warping an adult head surface to fit points measured on a neonatal head is a much more extreme test than the method which is used clinically, which is to warp one neonatal head surface to fit another. Results from such a test would be expected to be at least as good as, and probably better than, the results from the warped adult head mesh.

Acknowledgments

We would like to thank Andrew Bagshaw, Richard Bayford and Andrew Tizzard of the Department of Clinical Neurophysiology, University College London and the School of Health, Environment and Biological Sciences, Middlesex University, for providing the surface outline of the adult head.

References

- Arridge S R 1999 Optical tomography in medical imaging *Inverse Problems* **15** R41–R93
- Arridge S R and Hebden J C 1997 Optical imaging in medicine: II. Modelling and reconstruction *Phys. Med. Biol.* **42** 841–53
- Arridge S R, Hebden J C, Schweiger M, Schmidt F E W, Fry M E, Hillman E M C, Dehghani H and Delpy D T 2000 A method for 3D time-resolved optical tomography *Int. J. Imaging Syst. Technol.* **11** 2–11
- Bagshaw A P, Liston A D, Bayford R H, Tizzard A, Gibson A P, Tidswell A T, Sparkes M K, Dehghani H, Binnie C D and Holder D S 2003 Electrical impedance tomography of human brain function using reconstruction algorithms based on the finite element method *Neuroimage* at press
- Bluestone A Y, Abdoulev G, Schmitz C H, Barbour R L and Hielscher A H 2001 Three-dimensional optical tomography of hemodynamics in the human head *Opt. Exp.* **9** 272–86
- Bookstein F L 1989 Principal warps: Thin-plate splines and the decomposition of deformations *IEEE Trans. Pattern. Anal. Mach. Intell.* **11** 567–85
- Dimbylow P J 2002 Fine resolution calculations of SAR in the human body for frequencies up to 3 GHz *Phys. Med. Biol.* **47** 2835–46
- Ermer J J, Mosher J C, Baillet S and Leah R M 2001 Rapidly recomputable EEG forward models for realistic head shapes *Phys. Med. Biol.* **46** 1265–81
- Firbank M, Oda M and Delpy D T 1995 An improved design for a stable and reproducible phantom material for use in near-infrared spectroscopy and imaging *Phys. Med. Biol.* **40** 955–61
- Gibson A P 2000 Electrical impedance tomography of human brain function *PhD Thesis* University of London
- Gibson A P, Yusof R M, Dehghani H, Riley J, Everdell N, Richards R, Hebden J C, Schweiger M, Arridge S R and Delpy D T 2003 Optical tomography of a realistic neonatal head phantom *Appl. Opt.* **42** (16)
- Hebden J C, Gibson A P, Yusof R M, Everdell N, Hillman E M, Delpy D T, Austin T, Meek J and Wyatt J S 2002 Three-dimensional optical tomography of the premature infant brain *Phys. Med. Biol.* **47** 4155–66
- Hebden J C, Gonzalez F M, Gibson A P, Hillman E M, Yusof R M, Everdell N, Delpy D T, Zaccanti G and Martelli F 2003 Assessment of an in situ temporal calibration method for time-resolved optical tomography *J. Biomed. Opt.* **8** 87–92
- Hebden J C, Veenstra H, Dehghani H, Hillman E M, Schweiger M, Arridge S R and Delpy D T 2001 Three-dimensional time-resolved optical tomography of a conical breast phantom *Appl. Opt.* **40** 3278–87
- Hill D L, Batchelor P G, Holden M and Hawkes D J 2001 Medical image registration *Phys. Med. Biol.* **46** R1–R45
- Hillman E M C, Hebden J C, Schmidt F E W, Arridge S R, Schweiger M, Dehghani H and Delpy D T 2000 Calibration techniques and datatype extraction for time-resolved optical tomography *Rev. Sci. Instrum.* **71** 3415–27
- Huttenlocher D P, Klanderman G A and Rucklidge W J 1993 Comparing images using the Hausdorff distance *IEEE Trans. Pattern Anal. Mach. Intell.* **15** 850–63

- Nishitani N, Uutela K, Shibasaki H and Hari R 1999 Cortical visuomotor integration during eye pursuit and eye-finger pursuit *J. Neurosci.* **19** 2647–57
- Pogue B W, Giemer S, McBride T, Jiang S, Osterberg U L and Paulsen K D 2001 Three-dimensional simulation of near-infrared diffusion in tissue: boundary condition and geometry analysis for finite-element image reconstruction *Appl. Opt.* **40** 588–600
- Schmidt F E W, Fry M E, Hillman E M C, Hebden J C and Delpy D T 2000 A 32-channel time-resolved instrument for medical optical tomography *Rev. Sci. Instrum.* **71** 256–65
- Schöberl J 1997 NETGEN—An advancing front 2D/3D-mesh generator based on abstract rules. *Comput. Visual. Sci.* **1** 41–52
- Tidswell T, Gibson A, Bayford R H and Holder D S 2001 Three-dimensional electrical impedance tomography of human brain activity *Neuroimage* **13** 283–94